Metascience in Aerospace

Metascience in Aerospace, 1(2): 159–184.
DOI: 10.3934/mina.2024007
Received date: 27 November 2023
Revised date: 19 February 2024
Accepted date: 28 February 2024
Published date: 12 March 2024

https://www.aimspress.com/journal/mina

Theory article

Effects of oxygen concentration of oxidizer flow on laminar diffusion flame established over liquid fuel beds at microgravity

Hui Ying WANG* and Némo DECAMPS

Institut Pprime (CNRS-UPR 3346, ENSMA, Poitiers University), Département Fluide-Thermique-Combustion, ENSMA - BP 40109, Téléport 2, 1 av Clément ADER, 86961 Futuroscope Chasseneuil Cedex, France

Correspondence: Email: wang@ensma.fr; Tel: 33-549-498-295.

Abstract: The effects of oxygen concentration in oxidizer flow with a low speed of 0.1–0.3 m/s on a co-current flame spread over a thin liquid fuel bed at microgravity is numerically studied. The soot model is based on the Laminar Smoke Point (LSP) concept, which was used to reproduce the behaviour of a non-premixed, heavily sooting laminar flame. The results including flame patterns, soot emissions, temperature, and liquid burning rate are examined. Pyrolysis rate of liquid fuel significantly increases by increasing forced flow velocity and oxygen concentration, favouring flame length and soot formation. The flame behaviour at very low strain rates depends on both radiative heat loss and combustion efficiency, which are affected by oxygen concentration. The reactive boundary layer is significantly lifted along the pyrolysis surface due to lack of oxygen in the growing boundary layer, and the 3D effects are of importance due to thermal expansion. The ratio between the flame stand-off distance and the boundary layer thickness converges toward unity, however, the soot resides within the boundary layer. Compared to a heptane flame, a dodecane flame has lower pyrolysis rate and more effective oxygen transport ensures intensive combustion. A high oxidizer flow velocity results in a longer flame, and a reduction in flame standoff distance from the flat plate.

Key words: flame length; radiation loss; soot formation; flame stand-off; microgravity

Abbreviations: LSP: Laminar smoke point; HRR: Heat release rate (kW); HRRPUA: Heat release rate per unit area ($kW.m^{-2}$); RTE: Radiative transfer equation

Nomenclature listing

a	Arrhenius parameter in combustion model
A	pre-exponential factor in combustion model
A_f	pre-exponential factor in soot model
b	Arrhenius parameter in combustion model
d_f	flame stand-off distance (m)
D	diffusivity ($m^2.s^{-1}$)
E	activation energy
f	mixture fraction
f_v	soot volume fraction
h	sensible enthalpy ($kJ.kg^{-1}$)
k	thermal conductivity ($W.m^{-1}.K^{-1}$)
l	direction vector of the radiation
L	convective length scale (m)
L_f	horizontal flame length (m)
L_v	pyrolysis heat ($kJ.kg^{-1}$)
Lp	length of the pyrolysis area
$\dot{m}_s^{"}$	mass loss rate of liquid fuel per unit surface (kg.m-2s-1)
Nu	Nusselt number
N_Ω	number of solid angle.
p	pressure (Pa)
$\dot{q}_{conv}^{"}$	convection heat flux ($kW.m^{-2}$)
$\dot{q}_{rad}^{"}$	radiation heat flux ($kW.m^{-2}$)
$\dot{q}_c^{'''}$	heat release rate per unit volume ($kW.m^{-3}$)
$q_r^{"}$	radiative heat flux ($kW.m^{-2}$)
R	gas universal constant
s	stoichiometric coefficient
T	gas temperature (°C)
T_b	boiling temperature of liquid (K)
T_g	gas temperature (K) at the center of the adjacent gas phase cell
T_s	surface temperature of liquid (K)
t	time (s)
u	velocity ($m.s^{-1}$)
u_n	normal component of velocity at the surface
U_O	oxidizer flow velocity ($m.s^{-1}$)
Y_F	fuel mass fraction
$Y_{F,g}$	fuel mass fraction at the center of the adjacent gas phase cell
$Y_{F,s}$	fuel mass fraction at liquid surface
Y_O	oxygen mass fraction
Y_P	product mass fraction
Y_s	soot mass fraction
x, y, z	coordinates system in numerical simulation

W_F molar weight of liquid fuel ($kg.kmol^{-1}$)
W_m molar weight of mixture ($kg.kmol^{-1}$)
W_p width of the pyrolysis area

Greek

ρ volume density ($kg.m^{-3}$)
ρ_s gas volume density at the surface ($kg.m^{-3}$)
Ω solid angle
τ_{mix} key mixing timescale (s)
τ_{ij} viscous stress
μ laminar viscosity ($kg.m^{-1}.s^{-1}$)
κ absorption coefficient
κ_g gas absorption coefficient
κ_s soot absorption coefficient
δn distance between the surface and the center of the adjacent gas phase cell
$\dot{\omega}_{s,N}^{'''}$ soot inception rate ($kg.m^{-3}.s^{-1}$)
$\dot{\omega}_{s,O}^{'''}$ soot oxidation rate ($kg.m^{-3}.s^{-1}$)
ΔH_c energy released per kilogram of fuel consumed ($kJ.kg^{-1}$)
$\delta\Omega^l$ solid angle corresponding to direction l

1. Introduction

Buoyancy-induced flow at Earth-gravity is initially laminar, and transition to turbulence occurs when the fire is fully developed. Due to the absence of natural convection in spacecraft, a flame propagation over a condensed fuel surface by diffusion of heat and mass by forced convection is expected to be laminar [1]. Forced-flow flame spread in microgravity at low-velocity can't be reproduced on Earth, and flame radiation loss is significantly affected by Earth gravity via the time scales for chemical reaction and inviscid buoyant/viscous convections [2,3].

Radiation becomes the predominant mode of heat transfer via soot emissions for a co-current microgravity diffusion flame, which always resides within the boundary layer [4,5]. Soot formation and thus flame structure with a gas fuel in the absence of natural convection are affected by blowing effects [4,5]. A short residence time at high strain rates is the key factor for extinction of laminar diffusion flames via kinetic chemical processes. In microgravity, radiation loss becomes predominant to conduct extinction of gaseous diffusion at very low strain rates [6,7] due to absence of acceleration (strain) of the flow field by buoyancy. By neglecting radiation heat transfer, the analytical solution [8] is developed to describe the flat surface burning in a parallel stream of oxidizer in a reacting boundary layer. The exact solution [9] deals with the pyrolysis of solid fuel in the combustion chamber of a hybrid rocket. In order to overcome gravity effects in previous work [8,9], the flow velocity would have to be so large that the radiant flux from the flame approximately balances surface re-radiation, and that there is not an external heat flux, and then the forced-flow flame spread is primarily determined by convective heat flux. Numerical study demonstrated that the velocity overshoots close to the reacting zone at low-velocity flow in microgravity is a function of blowing and thermal expansion [10].

Many steady spread experiments over thin solids in both buoyant and forced flows have been carried out [11–18] for showing impact of flow velocity and oxygen concentration on the flame length. Only for a non-radiative flame, the heat flux at the solid fuel surface can be obtained from the solution of the laminar boundary layer diffusion flame [11,12]. It is found flame length increases when radiation losses are reduced, and the decrease of the heat flux with distance is dominated by the flame extension. By using forced flow models [11,13], a spread rate that increases with the flow velocity is predicted. For a two-dimensional (2D) sample, a steady spread with constant limiting length is predicted without flame radiation. As compared to the aforementioned results [13], other works [14,15] show that gas radiation modifies the flame length, spread rate, and flame extinction limit. Using a 2D transient model, flame spread with a limiting length in a forced low-speed flow, over both thin and thick solids surface, has been studied [16]. A finite sample width affects co-current flame spread over a condensed fuel plate [17,18].

Current knowledge is limited to flame development with a selected gas or solid fuel [1–18] as a function of oxygen concentration, flow rate, and pressure. This theoretical research looks specifically at the impacts of oxidizer flow conditions including oxygen concentration and its speed on a boundary diffusion flame established over liquid fuel beds at microgravity. Various liquid fuels, such as heptane and dodecane are considered, because they are commonly chosen in studies on fire behavior. Soot emission with a dependence on temperature and composition is apparently important due to long residence time in microgravity [19]. The rate of soot emission is limited by the growth of aromatics rather than the formation of the first ring [20]. Since the heterogeneous processes of soot inception and its surface growth are rather complex [21–25], several semi-empirical soot models [19,20,21] are currently used. A number of empirical parameters in inception, coagulation, and surface growth processes are only experimentally calibrated for ethylene, and they are not available for other fuel types such as heptane or dodecane. A simple soot conversion model used in Fire Dynamics Simulator (FDS, Version 6.7) [27] can't be directly applied to a heavily sooting, microgravity boundary layer flame. The novelty of this study is implementation of a Laminar Smoke Point (LSP) model [26] in the software package FDS6.7, which is developed by the National Institute of Standards and Technology, U.S. The model of laminar smoke point allows us to provide a general and practical solution for soot modeling in multi-fueled fires, such as heptane or dodecane fire, even when its exact elementary reactions are generally unknown. It is discovered that an increase in oxygen fraction and oxidizer flow velocity enhances soot formation, heat release rate (HRR) and gas temperature. The more fundamental research in these areas helps to improve spacecraft fire safety.

2. Numerical modelling and its validation

A brief description of the theoretical background and the essential physical processes in hydrodynamic, combustion, and soot models is presented. In manned spacecraft, velocities of ventilation drafts are of the order of 0.1 to 0.2 m/s. The peak buoyant flow induced by flames at Earth gravity at the flame base is about 0.3 m/s. Flame spread over a condensed fuel surface after incidental initiation by a heat source at a low Reynolds number co-current flow seems the most likely scenario. Absence of buoyancy in microgravity enables a boundary layer diffusion flame, as shown in Fig. 1a.

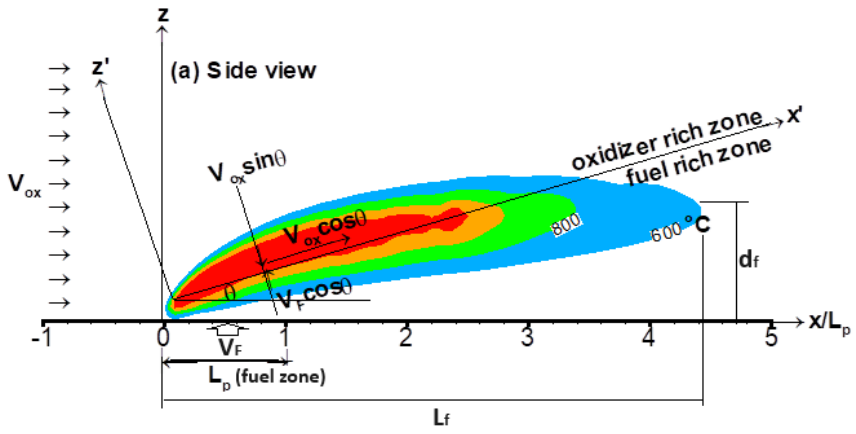

1a). Diffusion flame at side view.

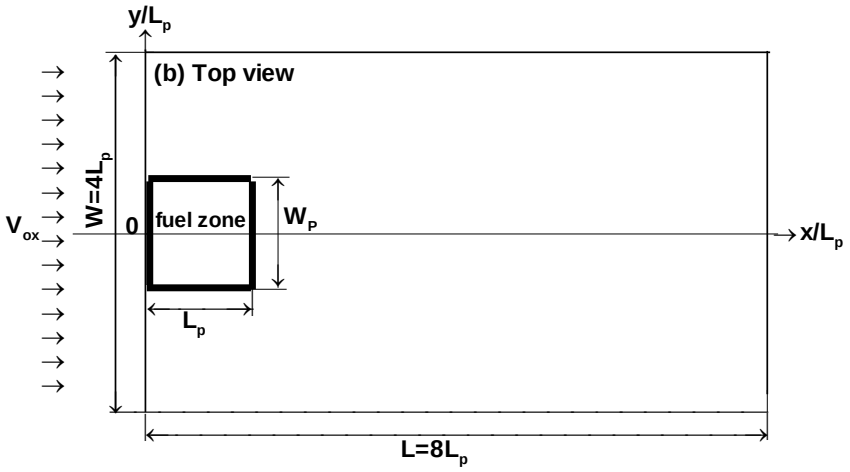

1b). Fuel zone disposition at top view.

Figure 1. Coordinate system of a boundary layer diffusion flame.

The starting point of the analysis is the set of the fully three-dimensional, unsteady reacting flow equations, which are discretized and iteratively solved. The physics-based model that governs the phenomena of interest here and the numerical methods are descripted in detail in the FDS6.7 user guide [27].

2.1. Hydrodynamic model

The hydrodynamic model consists of the transient equations of mass, momentum, energy, and species conservation.

Mass conservation:

$$\frac{\partial \rho}{\partial t} + \nabla \cdot (\rho u) = 0 \tag{1}$$

Momentum conservation:

$$\frac{\partial \rho u}{\partial t} + \nabla \cdot (\rho u u) = -\nabla p - \nabla . \tau \tag{2}$$

Energy conservation:

$$\frac{\partial \rho h}{\partial t} + \nabla \cdot (\rho h u) = \nabla \cdot (k \nabla T) + \dot{q}_c''' - \nabla \cdot q_r'' \tag{3}$$

Chemical species conservation:

$$\frac{\partial \rho Y_i}{\partial t} + \nabla \cdot (\rho Y_i u) = \nabla \cdot (\rho D \nabla Y_i) + \dot{\omega}_i''' \tag{4}$$

2.2. Combustion model

Because the pyrolyzed fuel and oxidizer are initially separated, the flame is primarily of the diffusion type. As shown in Fig. 1a, the separation of the pyrolyzed fuel and oxidizer is roughly schematized by a straight line behind the leading edge. A slope can be approximately estimated by the expression, $\tan\theta = d_f / L_f$ where d_f denotes the flame standoff distance and L_f the flame length. The flame length corresponds to the distance of the 600 °C contour from the leading edge, below which radiation loss is too low to affect the flame. The flame standoff distance is defined as the distance of the flame tip from the flat plate. At the location of the stoichiometric mixture fraction, fuel is transported with a velocity of $V_F \cos\theta$, and oxidizer with a velocity of $V_{ox} \cos\theta$ toward the mixing zone by convection, but within this zone diffusion determines the flame position. The flame thickness, ε, can be estimated from HRR where oxygen and fuel are delivered in stoichiometric proportions. The characteristic diffusion time is defined as

$$\tau = \frac{s \varepsilon^2}{D Y_{o,\infty}} \tag{5}$$

In the x' direction (see Fig. 1a), oxidizer and fuel separate from each other with a mixing velocity given by

$$V_{x'} = V_{ox} \cos\theta - V_F \sin\theta . \tag{6}$$

When the ratio, $R = \varepsilon / \tau V_{x'}$, is higher than unity, fuel and oxidizer arriving parallel to the x' axis will react. Inversely, for boundary layer diffusion flame at low velocity, the R value is lower than unity, implying that oxidizer will escape before being able to react with the fuel at a flame thickness, ε. As a result, unburnt hydrocarbons, CO, and soot are present in flame to some extent, which can be approximately determined by

$$L_{ext} = \tau V_F \sin\theta \tag{7}$$

To calculate CO and unburnt hydrocarbon, reactions from Westbrook [27] are assumed to account for carbon monoxide production via the two sequential, semi-global steps.

$$C_m H_n + \left(\frac{m}{2} + \frac{n}{4}\right) O_2 \rightarrow m\,CO + \frac{n}{2} H_2 O \tag{8}$$

$$CO + \frac{1}{2} O_2 \Leftrightarrow CO_2 \tag{9}$$

To avoid the modelling of a complex reaction mechanism of ignition processes, the primitive fuel oxidation (8) is considered as a mixing-controlled chemistry, and its reaction rate is calculated as

$$\dot{\omega}_F''' = \frac{d\rho Y_F}{dt} = -\frac{\rho}{\tau_{mix}} \min(Y_F, \frac{Y_O}{s}) \tag{10}$$

The key mixing timescale in Eq. (10), τ_{mix}, is supposed to relate approximately to the processes of diffusion and chemical reaction times [27]. The mixing-controlled chemistry is combined with a finite-rate reversible carbon monoxide reaction, and the Arrhenius parameters A, a, b, E are given in [28].

$$\dot{\omega}_{CO}''' = \frac{d[\rho Y_{CO}]}{dt} = -A\rho[Y_{CO}]^a [Y_O]^b e^{-E/RT} \tag{11}$$

The heat release rate in energy equation (3) is calculated from the fuel consumption rate,

$$\dot{q}_c''' = \dot{\omega}_F''' \Delta H_F + \dot{\omega}_{CO}''' \Delta H_{CO} \tag{12}$$

2.3. Soot formation model

According to the analysis in Eqs. 5 and 6, microgravity boundary layer flames have much greater tendencies to emit soot particulates. The processes of soot inception and oxidation are applied to the balance (see Eq. 4) between transport and soot production via the respective source terms:

$$\dot{\omega}_i''' = \dot{\omega}_{s,N}''' + \dot{\omega}_{s,O}''' \tag{13}$$

Laminar smoke point (LSP) concept [26] allows us to determine the soot inception rate.

$$\dot{\omega}_{s,N}''' = A_f \rho^2 T^{2.25} \frac{f - f_{st}}{1 - f_{st}} \exp(-2000/T) \tag{14}$$

where the pre-exponential factor, A_f, accounts for the sooting propensity of a specific fuel. The conserved Schvab-Zeldovich, mixture fraction, f, is the key scalar variable in the soot inception process.

$$f = Y_F + \frac{1 + Y_P}{s} \tag{15}$$

The sooting propensities of various fuels are accounted for via a pre-exponential factor A_f, which is in reversely proportional to its LSP height, L_{Fuel}.

$$\frac{A_{f,Fuel}}{A_{f,C_2H_4}} = \frac{L_{C_2H_4}}{L_{Fuel}} \tag{16}$$

A summary of A_f, calculated according to Eq. (16) for the used hydrocarbon fuels in the current work, is pre-tabulated in Table 1.

Table 1. Summary of the pre-exponential factor, A_f, for various fuels.

Fuel type	ethylene	heptane	dodecane
A_f	4.1×10^{-5}	2.9×10^{-5}	3.1×10^{-5}

The temperature dependence of soot oxidation in a laminar diffusion flame is modelled [26,27], and its specific rate is expressed as a function of soot and oxygen concentrations (mol/cm^3) by

$$\dot{\omega}_{s,O}''' = -4.7 \times 10^{10} [Ys][Yo] \exp(-211000/RT) \tag{17}$$

2.4. Radiative heat transfer model

For a heavily sooting flame such as fire, radiation is a crucial aspect of combustion, and can dominate other modes of heat transfer. A radiative transfer equation (RTE) is solved by using a ray-based method [27].

$$\vec{\nabla}.\vec{\Omega} I + \kappa I = \kappa \frac{\sigma T^4}{\pi} \tag{18}$$

Soot emission has a large influence on the radiation for low-flow-speed microgravity flame, and its effects are included with gas in the absorption coefficient.

$$\kappa = \kappa_s + \kappa_g \tag{19}$$

A spectral dependence of gas absorption coefficient κ_g [27] is taken into account for the contribution from gas-phase radiation of H_2O and CO_2. As the radiation spectrum of soot is continuous, its absorption coefficient is calculated solely as a function of the temperature, T, and soot volume fraction, f_v [27]:

$$\kappa_s = 1225 f_v T \tag{20}$$

Under the gray gas assumption, the gas phase contribution to the radiative loss term in the energy equation (3) is

$$-\nabla \cdot q_r'' = \kappa [U - 4\pi I_b] \qquad \text{and} \quad U = \int_{4\pi} I(x,s')ds' \tag{21}$$

Here, I_b is blackbody radiation intensity.

2.5. Heat balance at interface

A one-dimensional heat conduction equation for the thermally-thick condensed phase temperature $T_s(x,t)$ is applied in the direction x pointing into the liquid phase [27]. The boundary condition on the front surface of a liquid is established via a heat balance:

$$-k_s \frac{\partial T_s}{\partial x}(0,t) = \dot{q}''_{conv} + \dot{q}''_{rad} - \dot{m}''_s L_v \tag{22}$$

where the point x = 0 represents the surface of liquid. The convective heat flux, $\dot{q}''_{conv}$, at the surface is calculated from Fourier law.

$$\dot{q}''_{conv} = k\frac{T_g - T_s(0,t)}{\delta n} \tag{23}$$

where δn is the distance between the surface and the center of the adjacent gas phase cell. The net radiative heat flux on a diffusively reflecting and emitting wall is written as

$$\dot{q}''_{rad} = \sum_{l=1}^{N_\Omega} I^l_w \int_{\delta\Omega^l} (s' \cdot n_w) ds' \tag{24}$$

The radiant intensity at the wall, I^l_w, is found from resolution of the radiative transfer equation (RTE) [27].

Typically, evaporation temperature is smaller for liquid than solid fuels. This is an important distinction compared to the pyrolysis of solid fuel over its surface, which normally depends on a critical ignition temperature above 450 °C [12–15]. Evaporation rate of liquid fuel is usually derived from the Stefan diffusion equation as a function of mass fraction of liquid fuel in the gas phase, $Y_{F,i}$ [27,29].

$$\dot{m}''_F = \frac{\rho D}{L} Nu \, Ln\left[\frac{1-Y_{F,\infty}}{1-Y_{F,i}}\right] \tag{25}$$

The formulation (25) does not contain the basic assumption for phase transitions in liquid evaporation, and solely an equilibrium state, which is the worst case in fire safety, is taken into account. The mass fraction of fuel vapor at the interface, $Y_{F,i}$, is derived from the Clausius-Clapeyron relation with a dependence on its surface temperature, T_s, and boiling temperature, T_b, as follows:

$$Y_{F,i} = \frac{W_F}{W_m} \exp\left[-\frac{L_v W_F}{R}\left(\frac{1}{T_s} - \frac{1}{T_b}\right)\right] \tag{26}$$

The mass balance at the burning boundary is established as

$$\dot{m}''_F = u_n \rho_s Y_{F,s} - (\rho D)_s \frac{Y_{F,g} - Y_{F,i}}{\delta n} \tag{27}$$

where u_n is the normal component of velocity at the surface pointing into the flow domain.

Table 2. Thermo-physical and combustion properties of heptane and dodecane.

Property	Heptane	Dodecane
Conductivity, k (W/m.K)	0.17	0.14
Density, ρ (kg/m^3)	684	750
Heat capacity, C_p (kJ/kg.K)	2.24	2.21
Pyrolysis heat, L_v (kJ/kg)	321	256
Heat of combustion, ΔH_c (kJ/kg)	44500	44147
Boiling temperature, T_b (°C)	98	216

For a laminar flame, material diffusivity, D, thermal conductivity, k, and viscosity, μ, are approximated from kinetic theory [27] as a function of temperature. The detailed information about the thermo-physical and combustion properties of heptane and dodecane are provided in Table 2 [29].

2.6. Computational domain and boundary conditions

The numerical simulation is achieved according to the experimental configuration [4,5]. Due to the limited space and amount of feed gases available in parabolic flight facilities, only a small square porous burner with dimensions of $L_p = W_p = 5$ cm with gas fuel (ethylene) supply of 5 (g/m^2s) is used. This allows us to avoid the coupling of heat feedback with condensed fuel so that longer experimentation time can be achieved. The gas burner is embedded in a stainless-steel plate at z=0 with a short entrance length of 5 cm. In the previous studies [10,30] on such a diffusion flame (see Fig. 1a), it was found that *a priori* estimates of the computational domain of $8L_p$ in the windward direction (x), and $4L_p$ in both the lateral (y) and normal (z) directions, seems to be enough to apply zero gradient conditions on the free boundaries such as at two sides, top and outlet of the domain for the farfield boundary values of the variables. An excessive domain extension needs the use of a highly compressed grid system, and build-up of numerical error could produce spurious results over the course of a calculation [27]. In the experiment, the oxidizer flow is with an elevated oxygen concentration of 35% and 50%, and a constant velocity, U_o, of 0.2 m/s was prescribed at the inlet of $x/L_p = -1$. Over the burning surface, a heat balance is established at the interface (see Eq. 22).

2.7. Model validation

Validation of the numerical model is achieved from the measured soot volume fraction with an experimental set-up, as displayed in Fig. 1. The soot volume fraction of ethylene laminar diffusion flame in microgravity is measured by using the laser induced incandescence technique (LII) [4,5]. The basic principle of this method relies on the detection of the thermal radiation from the soot particles that were heated up to vaporization temperature thanks to high energy laser pulse. The LII intensity image is later converted to soot volume fraction distribution, and the measurement accuracy depends on a proportionality constant, which is required for correction due to attenuations of both the laser beam and the collected signal. However, in the current numerical work, we lack the ability to quantitatively specify the measurement errors. The methodology and a valid approximation for the determination of the soot volume fraction in the microgravity flame are detailed in previous work [4,5].

A proper cell sensitivity analysis by varying the grid spacing from 2 to 1 mm was performed on the predicted quantities in the previous study [30]. A deviation of roughly 5% is observed for the flame temperature solely near the leading edge by varying the grid spacing from 2 to 1 mm. The computational domain consists of multiple meshes, which can be treated with 20 processors through parallel processing of a Linux cluster. The grid system contains 200 x 100 x 75 cells, and a typical simulation with a mesh size of 2 mm for a physical time of 10 s requires roughly 150 CPU hours. A reduction in the grid size to 1 mm results in a significant reduction in the time step ($\Delta t < 10^{-5}$ s) due to the Courant-Friedrichs-Lewy, the Von Neumann, and the realizable mass density constraints [27]. These three constraints on the time step are imposed in FDS6.7 [27] for maintaining numerical

stability and accuracy in the presence of advection, diffusion, and expansion of the velocity and scalar fields. With each halving of the grid size, the time required for the simulation increases to 150 x 2^4 CPU hours (a factor of two for each spatial coordinate, plus time), making practical flame simulations difficult. Although the thickness of a laminar flame is about 1 mm, a mesh size of 2 mm is extensively used for a low Reynolds number flow [10,30], because it is considered as the best trade-off between accuracy and cost for a three-dimensional reacting flow simulation.

Given in Figs. 2 and 3 is the comparison between the computed and measured soot volume fractions along the centreline across the height, z, at various axial locations x/L_p = 0.5–2.4. In comparison with the experimental data, the soot peak value (about 10 ppm) and its profile are numerically reproduced only for Y_o=0.35 (see Fig. 2). For a high oxygen concentration of 0.5 (see Fig. 3), the computations over-predict the soot peak present in the experiment for $x/L_p < 1.25$ and under-predict the peak value beyond that region ($x/L_p > 1.25$). The measured peak is located just above the burner surface with 1 mm, while the calculated one occurs with 2 mm. In all the cases, the numerical model predicts a stronger soot emission than that of the measurement. This is partially attributed to soot oxidation via the radicals OH, which can't be included in the two sequential, semi-global chemical reactions (see Eqs. 8, 9), especially for elevated oxygen concentration of 0.5. The comparison is deemed satisfactory with an uncertainty within 20% for $Y_o < 0.35$, considering all the simplifying assumptions made in the global soot model and uncertainties in measuring local soot concentration in microgravity conditions during parabolic flights. In spite of the difference between the numerical and the experimental results, any attempt to calibrate the empirical parameter in the soot model for matching the experimental data is discouraged due to lack of the model generalizability. As the recent results of such studies available in the work [19], verification of the results with experimental data for microgravity flame also shows some uncertainty in the soot model. In the following section, oxygen concentration is limited to 0.35 because a relatively good estimation of soot emission allows us to properly calculate the contribution of the radiation heat flux over the liquid surface in the vitiated air boundary layer.

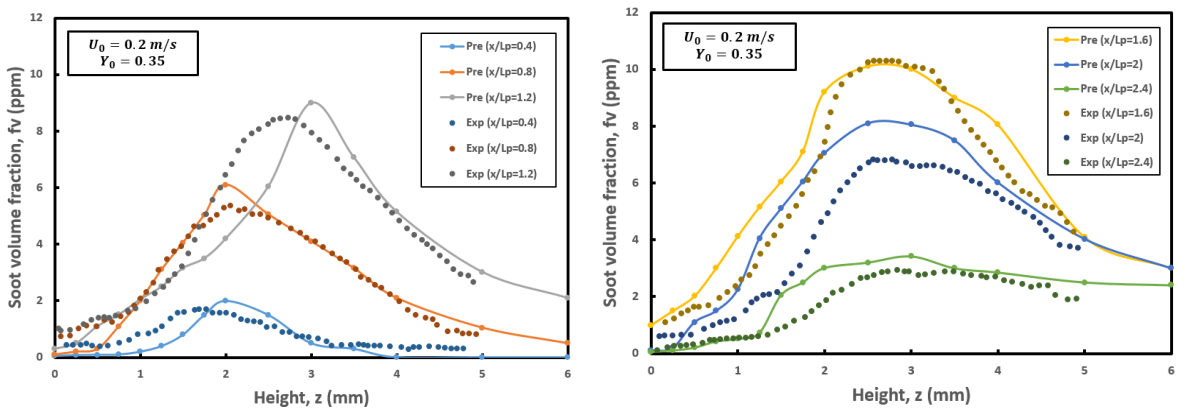

Figure 2. Profiles of soot volume fraction from prediction and measurement along the height z for ethylene flame at different locations at Y_o = 0.35.

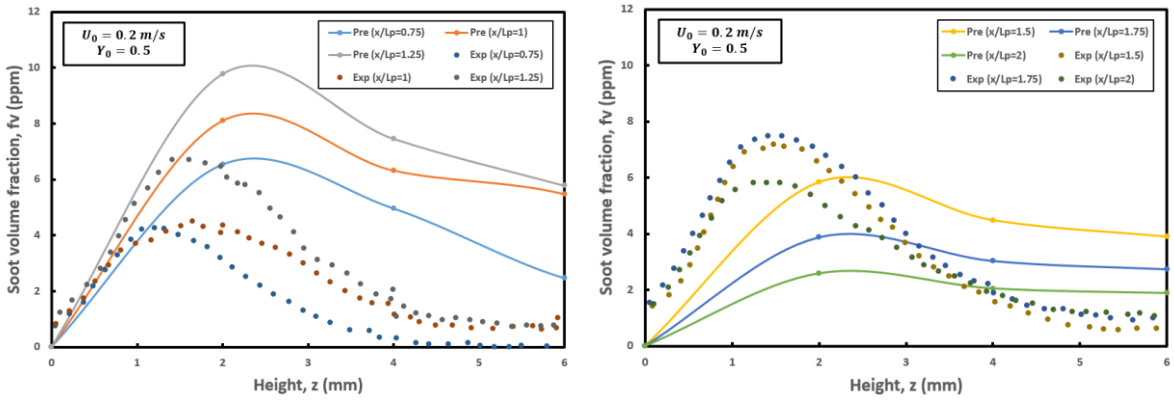

Figure 3. Profiles of soot volume fraction from prediction and measurement along the height z for ethylene flame at different locations x/L_p at $Y_o = 0.5$.

3. Results and discussions

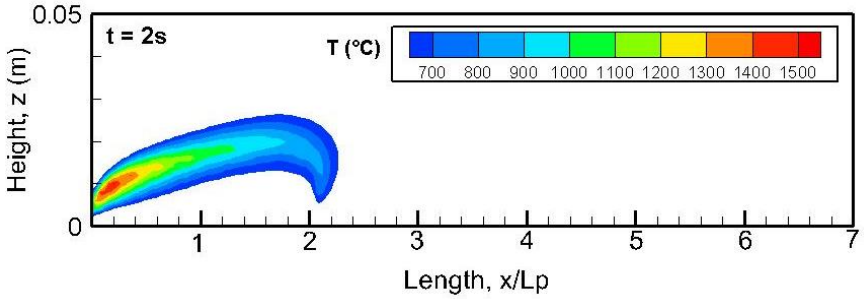

4a). Heptane.

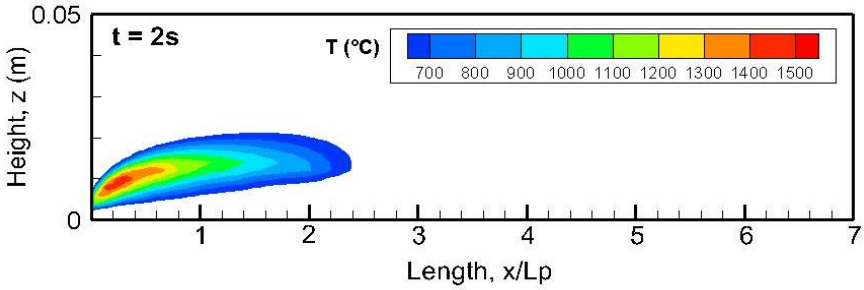

4b). Dodecane.

Figure 4. Co-current flame propagation over pyrolysis zone for $Y_o = 0.35$ and $U_0 = 0.2$ m/s at t = 2 s.

As an illustration, Figs. 4 and 5 are composed of two flame images in cross-stream plane at the growth period (t = 2 s) and the steady state (t = 10 s) for cross flow velocity of $U_0 = 0.2$ and oxygen fraction of $Y_O = 0.35$. In the growth period (t = 2 s), the strong burning rate of the heptane flame causes distortions of the temperature distribution at the flame tip. The flame length, L_f (see Fig. 1a), increases progressively with time during the growth period due to an increase in the pyrolysis rate of liquid fuel. The flame reaches a steady non-propagating state at about 10 seconds (see Fig. 5). A

lengthening of the flame is immersed in the developing flow boundary layer, and in parallel, the boundary layer flame is significantly lifted above the flat plate downstream from the pyrolysis zone ($x/L_p > 1$). In microgravity, the flame presents a remarkable augmentation in both the flame length (L_f) and the stand-off distance (d_f). Evaporation temperature is smaller for heptane than dodecane (see Tab. 2), thus flame length is higher than that of dodecane by a factor of 1.7 times at the steady state (t = 10 s).

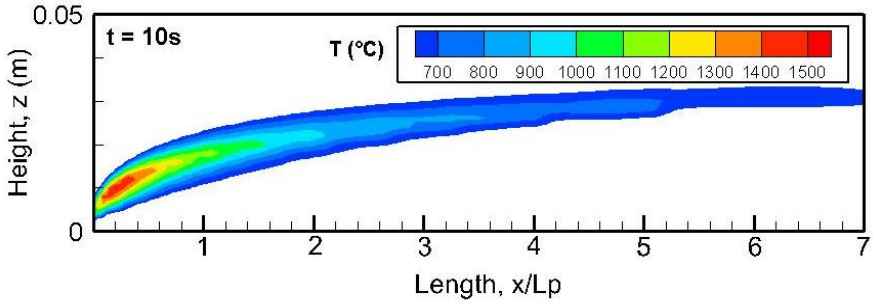

5a). Heptane.

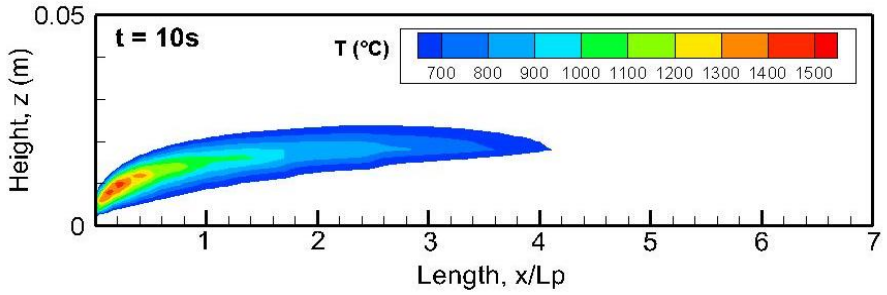

5b). Dodecane.

Figure 5. Co-current flame propagation over pyrolysis zone for $Y_o = 0.35$ and $U_0 = 0.2$ m/s at t = 10 s.

The virgin liquid fuel is preheated due to heat feedback from the post-combustion gases, and the flame acts as the source of gas ignition of the pyrolyzate and oxidizer mixture. The heated liquid layer lies near the surface without natural convection. Plotted in Fig. 6(a, b) are the pyrolysis rate distributions over the sample surface of heptane and dodecane at the various physical times at $U_0 = 0.2$ m/s and $Y_o = 0.35$. For heptane (cf. Fig. 6a) with a boiling point of 98 °C, sufficient volatiles are generated when the surface temperature is above 50 °C for sustaining a burning flame. However, for dodecane (see Fig. 6b) with a boiling point of 216 °C (see Tab. 2), volatiles become insufficient to sustain a burning flame in the region beyond $x/L_p > 0.5$ where its surface temperature is below 130 °C. The liquid pyrolysis rate varies significantly along the pyrolysis zone with a peak downstream of the leading edge due to the smallest flame standoff and thus the greatest heat feedback to the fuel. The pyrolysis rate (see Fig. 6) curve follows a growing trend with a rise of liquid temperature, and asymptotically reaches a constant peak downstream of the leading edge after a quasi-steady state is reached.

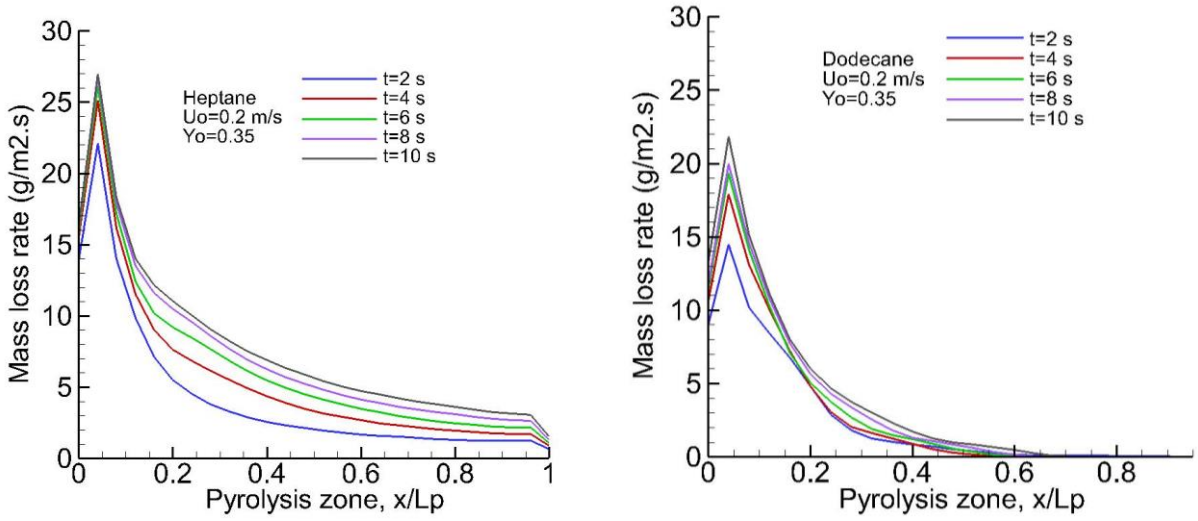

6a). Heptane. **6b**). Dodecane.

Figure 6. Calculated pyrolysis rate along heptane and dodecane surfaces for the various times at U_0=0.2 m/s.

Impact of oxygen fraction in addition to oxidizer flow velocity on the pyrolysis rate of heptane and dodecane at steady state is illustrated in Figs. 7(a, b) and 8(a, b). In microgravity, a diffusion flame is immersed in a vitiated air boundary layer, and consequently, an increase of oxygen fraction from 0.25 (see Fig. 7) to 0.35 (see Fig. 8) causes a sudden increase of pyrolysis rate by a factor of about 60% for heptane and about 80% for dodecane. Typically, boiling temperature is smaller for heptane than dodecane, thus the pyrolysis rate of heptane is higher. At $Y_o = 0.35$, the mass loss rate exhibits a peak of 32 g/m^{2}s for heptane and 22 g/m^{2}s for dodecane at $U_0 = 0.3$ m/s. A sharp decrease of pyrolysis rate beyond the leading edge is attributed to an insufficient heat feedback from the flame due to an important flame stand-off distance (see Fig. 5). For dodecane flame, the results indicate that less pyrolysis distance is reached at the steady state with a limiting pyrolysis length. The weak surface radiation heat flux from dodecane flame results in a limiting pyrolysis length, which is similar to those we see for solid fuel [16]. Length of the burning surface of dodecane is mainly proportional to crossflow speed, and its pyrolysis front length increases from $x/L_p = 0.4$, 0.6 to 0.8 with a rise of crossflow velocity from 0.1 to 0.3 m/s.

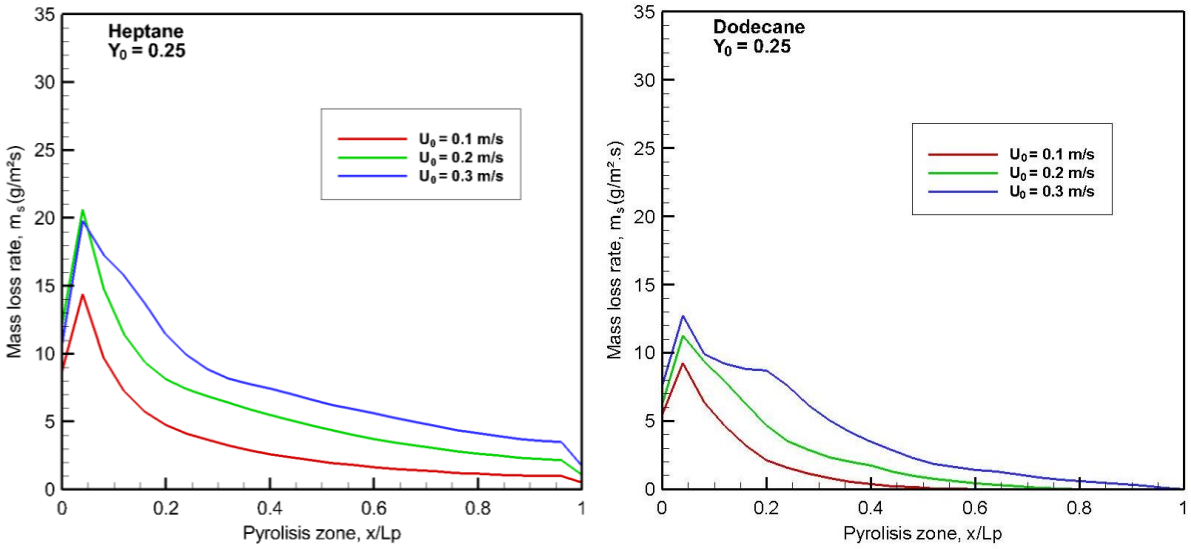

7a). Heptane. **7b**). Dodecane.

Figure 7. Mass loss rates of heptane and dodecane at $Y_o = 0.25$ for crossflow velocity varying from 0.1 to 0.3 m/s.

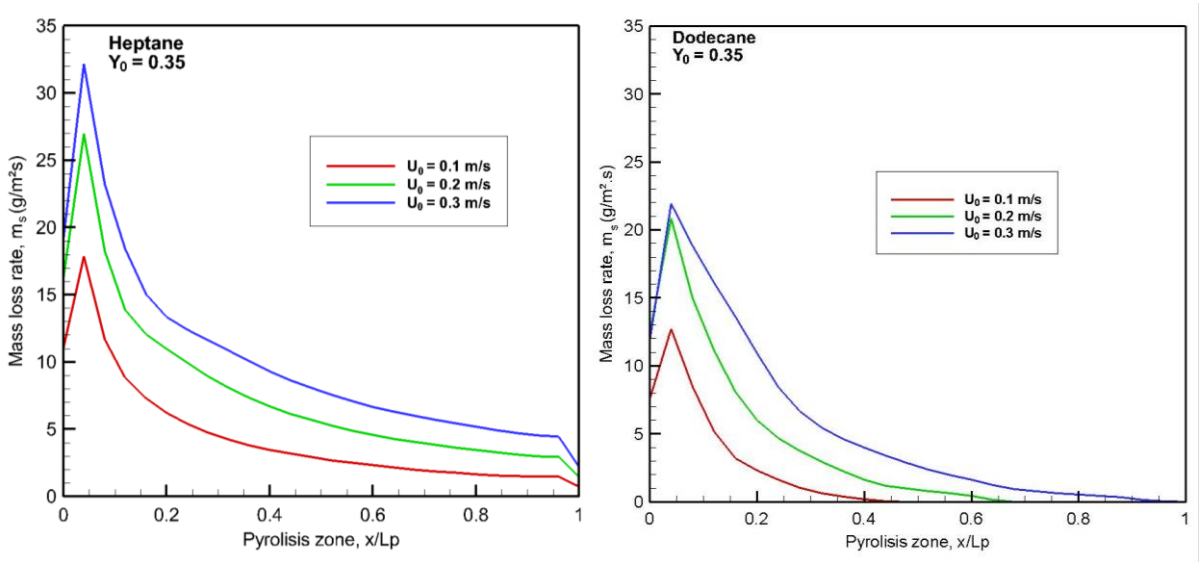

8a). Heptane **8b**). Dodecane

Figure 8. Mass loss rates of heptane and dodecane at $Y_o = 0.35$ for crossflow velocity varying from 0.1 to 0.3 m/s.

Figs. 9, 10, 11 and 12(a, b) are composed of a series of flame shapes in the windward plane and in cross-section ($x/L_p = 2$) for crossflow velocity of 0.1 and 0.3 m/s and two oxygen concentrations of $Y_O = 0.25$ and 0.35. The curvature of the leading edge corresponding to a peak of pyrolysis rate with a parabolic nature is more pronounced for U_0=0.1 m/s (see Figs. 7, 8). The flame slope angle, θ, as shown in Fig.1a, decreases with an increase of U_0. The inclination of the flame near the leading

edge is slightly affected by the oxygen concentration, but the flame length increases with an augmentation of Y_O from 0.25 to 0.35. However, an increase in the flame length is more remarkable with an increase of crossflow velocity compared to an increase of oxygen fraction. The leading edge remains attached to the pyrolysis surface, and the flame is fully lifted from the flat plate downstream in spite of both crossflow speed and oxygen concentration. The flame stand-off distance in microgravity increases by a factor of roughly 10 times compared to that described by Emmons [31] for a reacting boundary layer flow. An important standoff distance of microgravity flame is attributed to the greater importance of boundary layer diffusion as compared to expansion and convection. Length of heptane flame increases by a factor of 1.8 times as compared to a shorter flame length of dodecane due to its limiting regression zone (see Figs. 7b, 8b).

Due to spatially limited experimental volumes in microgravity, the two-dimensional flame behaviours were usually illustrated [4,5]. As shown in Figs. 9–12b, the flame behavior in the cross-section downstream of the trailing edge at the axial location of $x/L_p = 2$ displays a 3D behaviour. A stable symmetrical flame is generated in the cross-section. The extent of the thermal plume (T>600°C) in the cross-stream plane exceeds the pyrolysis zone with $-0.5 < y/L_p < 0.5$. The 3D effects downstream of the tailing edge are of importance with an increase of cross flow velocity. The flame exhibits a complex curved front due to thermal expansion in the lateral dimension. A low velocity of 0.1 m/s shortens the flame with the substantially low temperature at the same cross-section.

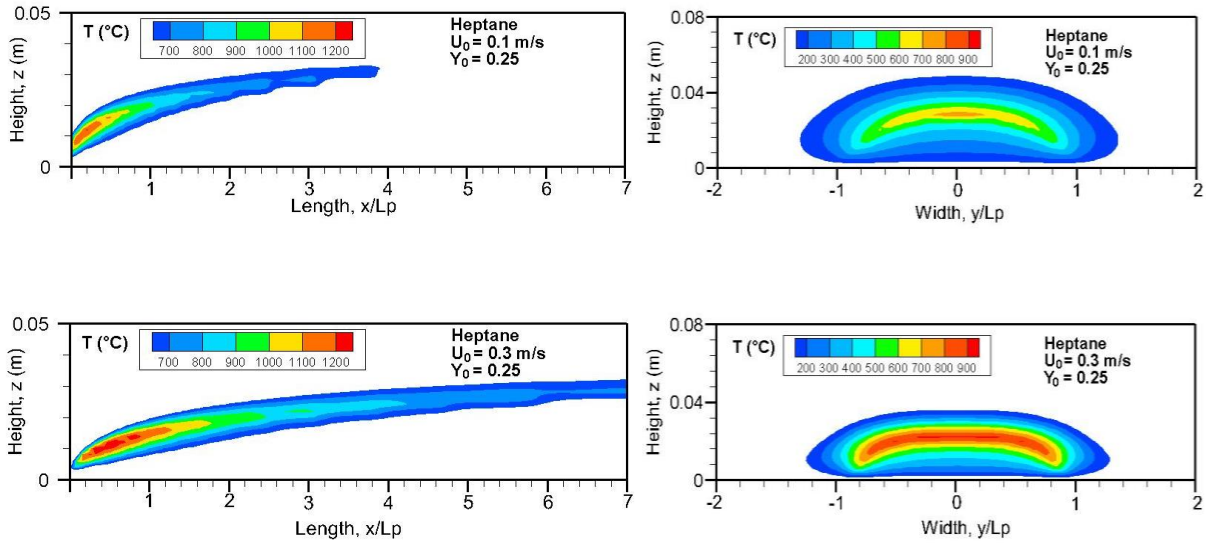

9a). Windward plane. **9b**). Cross-stream plane ($x/L_p = 2$).

Figure 9. Iso-contours of gas temperature for heptane at $Y_o = 0.25$ and $U_0 = 0.1$, 0.3 m/s.

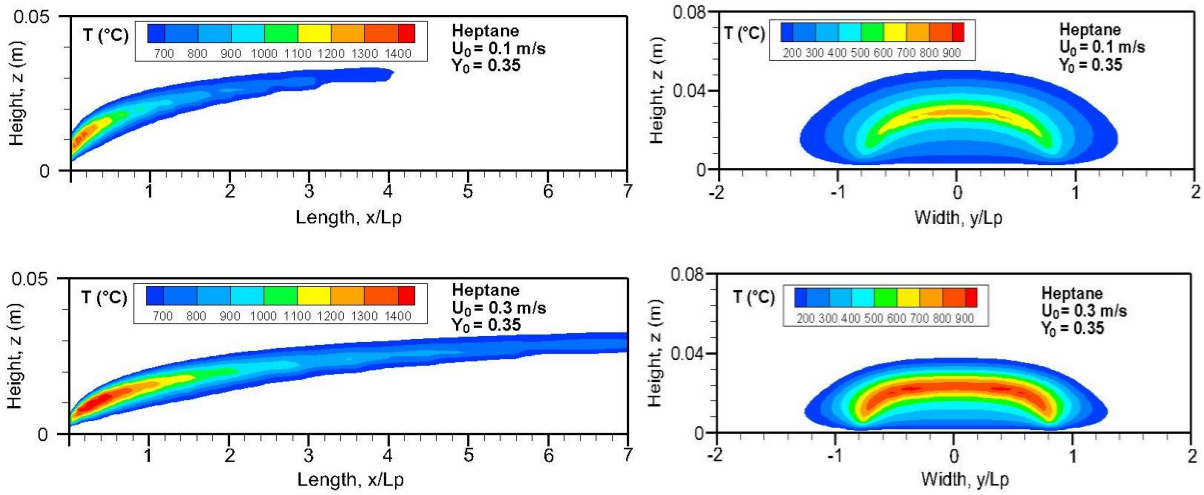

10a). Windward plane **10b**). Cross-stream plane ($x/L_p = 2$)

Figure 10. Iso-contours of gas temperature for heptane at $Y_o = 0.35$ and $U_0 = 0.1$, 0.3 m/s.

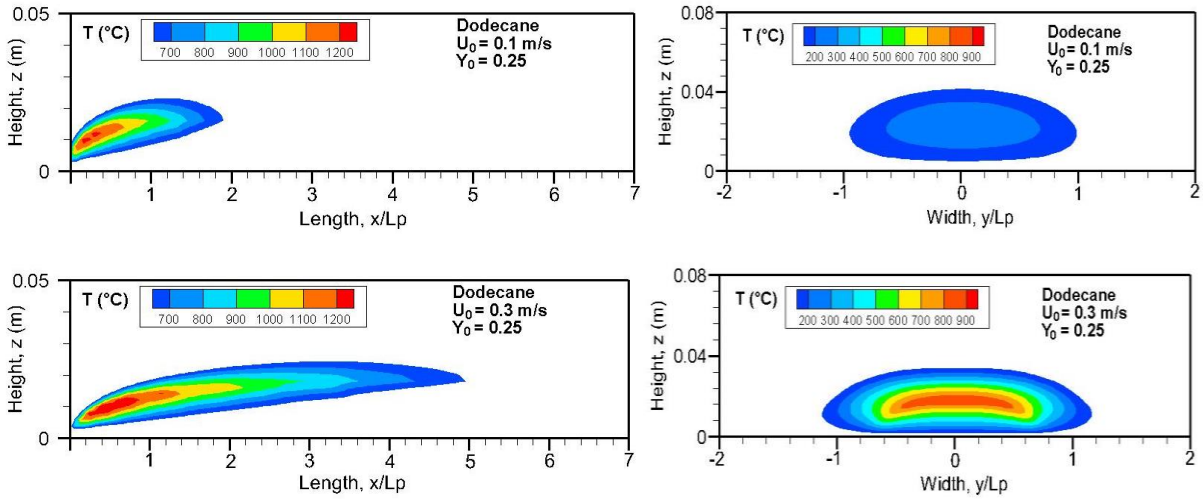

11a). Windward plane **11b**). Cross-stream plane ($x/L_p = 2$)

Figure 11. Iso-contours of gas temperature for dodecane at $Y_o = 0.25$ and $U_0 = 0.1$, 0.3 m/s.

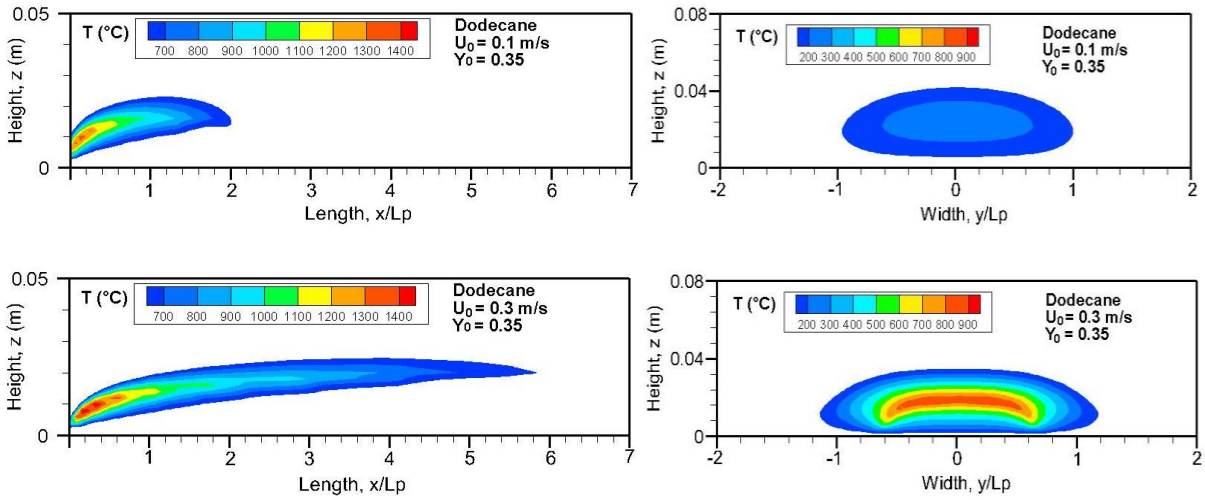

12a). Windward plane **12b**). Cross-stream plane ($x/L_p = 2$)

Figure 12. Iso-contours of gas temperature for dodecane at $Y_o = 0.35$ and $U_0 = 0.1$, 0.3 m/s.

Fig. 13a clearly shows that the flame temperature peak at the leading edge is strongly dependent on both crossflow velocity and oxygen fraction. The heat released by combustion induces a rise of the gas temperature above 1200 °C near the leading edge where less soot is formed. The predicted reactive zone is located at the locus of the heat release zone, corresponding to a peak temperature that continuously falls off with a drop of approximately 300 °C with a decrease of oxygen concentration from 0.35 to 0.25 at a fixed U_0. The general behaviour of the flame includes a strong augmentation of temperature peak with an increase of crossflow velocity from 0.1 to 0.3 m/s due to an increase of combustion intensity.

The combustion efficiency can be estimated from the ratio between the effective and theoretical HRRs,

$$\eta = \frac{Q_E}{Q_T} \tag{28}$$

Integration of the local heat release rate from the combustion model (see Eq.12) over all cells with a volume ΔV in the computation domain allows us to monitor the effective heat release rate,

$$Q_E = \sum (\dot{\omega}_F''' \Delta H_F + \dot{\omega}_{CO}''' \Delta H_{CO}) \Delta V \tag{29}$$

The theoretical HRR, Q_T, is determined from the pyrolysis rate of liquid fuel over the pyrolysis area,

$$Q_T = \dot{m}_s'' L_p W_p H_c \tag{30}$$

It is shown in Fig. 13b that a limiting pyrolysis zone of dodecane allows an improvement of combustion efficiency as a consequence of low fuel supply rate and decreases monotonically with U_0. A large pyrolysis rate of heptane due to great heat feedback in a high flame temperature region results in a decrease of combustion efficiency as a consequence of an excessive fuel supply to the boundary layer. In all the cases, the combustion efficiency is falling off with a decrease of oxygen concentration.

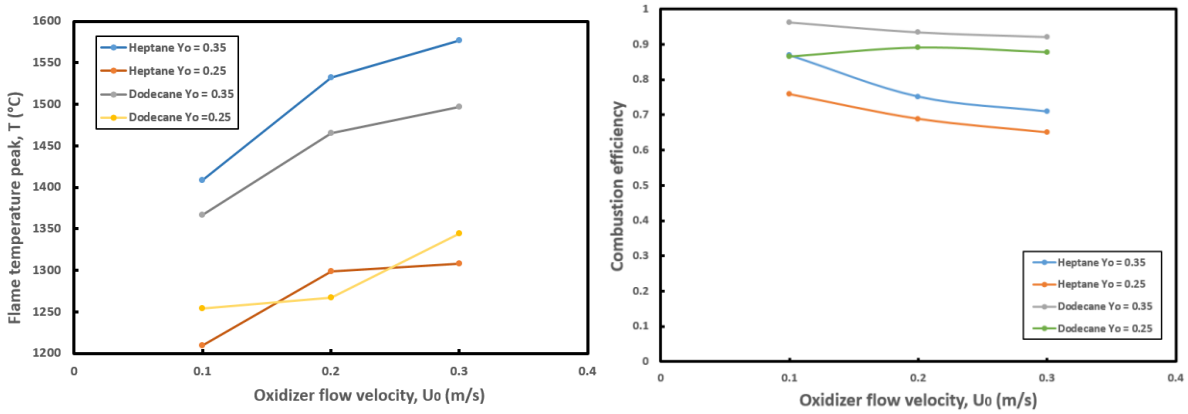

13a). Temperature peak. **13b**). Combustion efficiency.

Figure 13. Evolution of the temperature peak and combustion efficiency for heptane and dodecane as a function of oxidizer flow velocity U_0 = 0.1, 0.2, 0.3 m/s at Y_O = 0.35, 0.25.

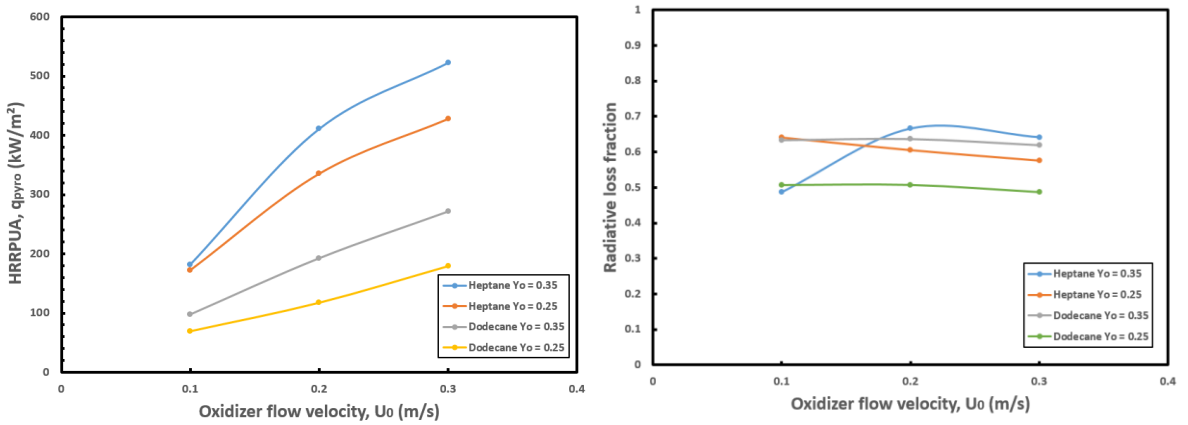

14a). HRR per unit area. **14b**). Radiative loss fraction.

Figure 14. Evolution of the HRR per unit area and radiative loss fraction for heptane and dodecane as a function of oxidizer flow speed at Y_O = 0.25 and 0.35.

Generalizability of the theoretical HRR, Q_T, at the steady mode from a reduced scale experimental device can be preserved by normalizing its value over the pyrolysis area (L_p x W_p, see Fig. 1b), giving heat release rate per unit area (HRRPUA), q_{pyro} (kW/m^2). Examined in Fig. 14a is the response of the HRRPUA to the change in cross-flow velocity, U_o, for oxygen concentration of 0.25 and 0.35. Typically, the HRRPUA increases by a factor of about 2.3 times with a rise of crossflow speed from 0.1 to 0.3 m/s, and of about 25% with an increase of oxygen concentration from 0.25 to 0.35. By using the radiative heat loss rate, Q_R, which is determined from the radiation model (see Eq. 18), and the theoretical HRR, Q_T, the radiative fraction, Q_R/Q_T, can be plotted versus U_0 in Fig. 14b for oxygen concentration of 0.25 and 0.35 at various velocity, U_0. At Earth gravity, the radiative loss fraction is lower than 0.35 due to weak soot formation because buoyancy enhances mixing and reduces residence times. A reduced convective flow in microgravity makes the radiative loss more

prominent to trigger flame extinction [6,7]. The radiative fraction is a temperature-sensitive volumetric loss mechanism in the visible flame region, which can be estimated by

$$V_{f,visible} = L_f \times \delta_f \times W_f \tag{31}$$

where L_f, δ_f, and W_f denote, respectively, length, thickness, and width of the visible flame (T > 600 °C), as shown in Figs. 9–12. The radiative fraction is higher than 0.5 and increases rapidly with U_0 for heptane flame at $Y_o = 0.35$ (see Fig. 14b) due to the presence of large soot particles in the combustion products. The emitted radiation is greater at a higher oxygen concentration of 0.35 due to increase in the visible flame volume, resulting in the greater radiation loss, which is practically independent of oxidizer flow rate except at $Y_o = 0.35$.

Effect of fuel injection rate, U_F, in the reactive boundary layer is described by a dimensionless volume coefficient, $C_q = U_F/U_O$ [32]. In the current work, since the pyrolysis rate varies over the liquid surface, the C_q can't be used as a constant. The ratio, d_f/d_r, between the flame sheet distance, d_f, and the reactive boundary layer thickness, d_r, is shown in Figs. 15 and 16 at $Y_O = 0.25$ and 0.35 for various oxidizer flow speeds, U_0. The flame sheet distance, d_f, is the one between the peak temperature and the pyrolysis surface corresponding to the maximum HRR. The flame leading edge is attached to the pyrolysis surface, and the flame sheet establishes at the limit of the viscous boundary layer. Both d_f and d_r are significantly lifted above the pyrolysis surface with a ratio, d_f/d_r, close to unity. Nevertheless, the peak temperature is slightly away from the stoichiometric line where the HRR reaches the maximum due to the radiation loss. The flame sheet thickness along the stoichiometric line is estimated to be $\varepsilon \approx 1.2\,\text{mm}$, with a duration of combustion of $\tau \approx 0.22\,s$ from Eq. 5, where both are practically independent of the free-stream velocity and oxygen concentration. The predicted thickness of the visible flame, δ_f (600 °C contour), as shown in Figs. 9–12, reaches a value of roughly 10 mm, which is about 9 times that of the flame sheet, ε.

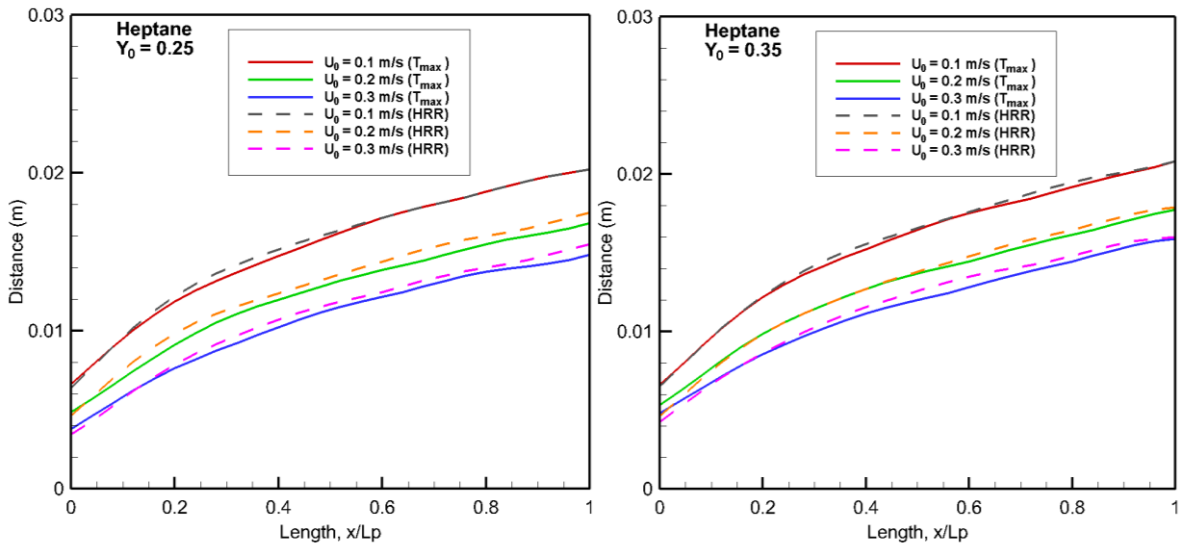

Figure 15. Evolution of the position of the flame sheet and boundary layer for heptane for different oxidizer flow velocity at $Y_O = 0.25$ (left) and 0.35 (right).

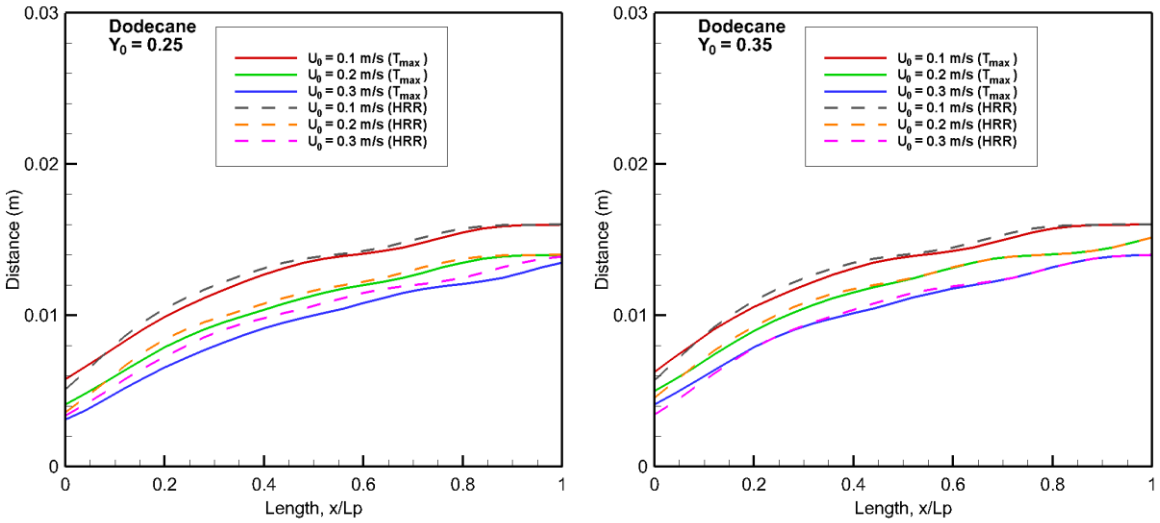

Figure 16. Evolution of the position of the flame sheet and boundary layer for dodecane for different oxidizer flow velocity at Y_O = 0.25 (left) and 0.35 (right).

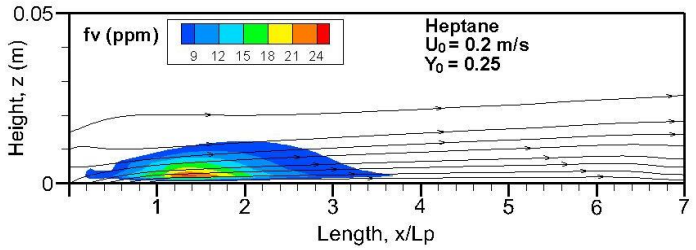

17a). Y_o = 0.25

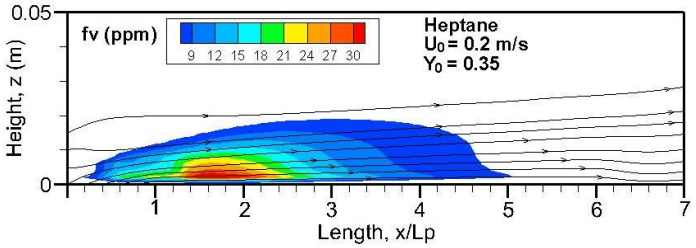

17b). Y_o = 0.35

Figure 17. Impact of two oxygen concentrations at Y_o = 0.25 and 0.35 on fields of soot volume fraction in addition to the windward streamlines for heptane at U_0 = 0.2 m/s.

As an illustration, the impact of the oxygen concentration on fields of soot volume fraction for heptane in the windward plane on the axis of symmetry at U_0 = 0.2 m/s is presented in Fig. 17(a, b) for oxygen concentration of 0.25 and 0.35. A similar trend is found for dodecane flame. Significant soot emission takes place over the pyrolysis zone where the fuel is rich and temperature is high, and its amount depends significantly on the liquid fuel type. At Earth gravity, the buoyancy-induced

convection transports soot toward the flame sheet for burning it, and the dominant diffusion or thermal expansion at microgravity prevents soot particles from approaching the flame sheet due to the thermophoretical effects [33], independent of the mainstream flow conditions. At low speed forced flow, soot is immersed below the diffusion flame sheet close to the free flow velocity. The smaller effective crossflow velocity helps to amplify the lateral mixing and cooling of thermal plume via soot emission. The three-dimensional features of soot on the cross-stream section for heptane at the axial location of $x/L_p = 2$ are illustrated in Fig. 18(a, b) for oxygen concentration of 0.25 and 0.35. The extent of the soot emission in the cross-stream plane is located inside the pyrolysis width ($-0.5 < y/L_p < 0.5$).

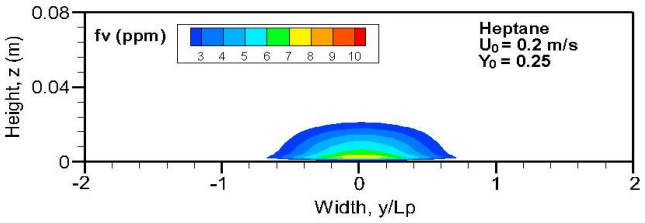

18a). $Y_o = 0.25$.

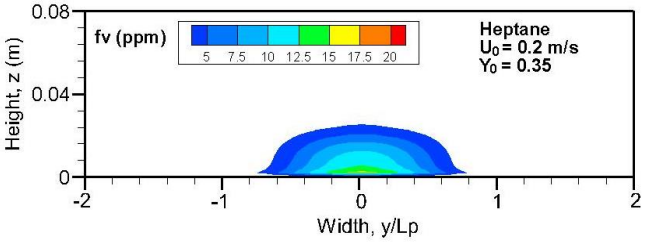

18b). $Y_o = 0.35$.

Figure 18. Impact of two oxygen concentrations at $Y_o = 0.25$ and 0.35 on fields of soot volume fraction in the cross-stream plane ($x/L_p=2$) for heptane at $U_0 = 0.2$ m/s.

Evolution of the mean soot formation, which is averaged through the integrated smoke layer, along the windward direction is examined in Fig. 19(a–d). An increase of oxygen fraction or oxidizer flow velocity leads to an enhancement of soot in the peak. The peak of the mean soot emission takes place downstream of the trailing edge at $x/L_p = 2$ for heptane, and at $x/L_p = 0.5$ for dodecane flame, beyond which its pyrolysis rate remains rather small (see Fig. 7b, 8b). As compared to dodecane flame (see Fig. 19b, d), the heptane flame (see Fig. 19a, c) seems heavily sooting with an augmentation by a factor of roughly 3.5 times at low flow velocity of 0.1 m/s. Strong pyrolysis rate and high temperature with oxygen concentration of 0.35 seem ideal for formation of an important thickness of smoke layer due to an excessive fuel supply.

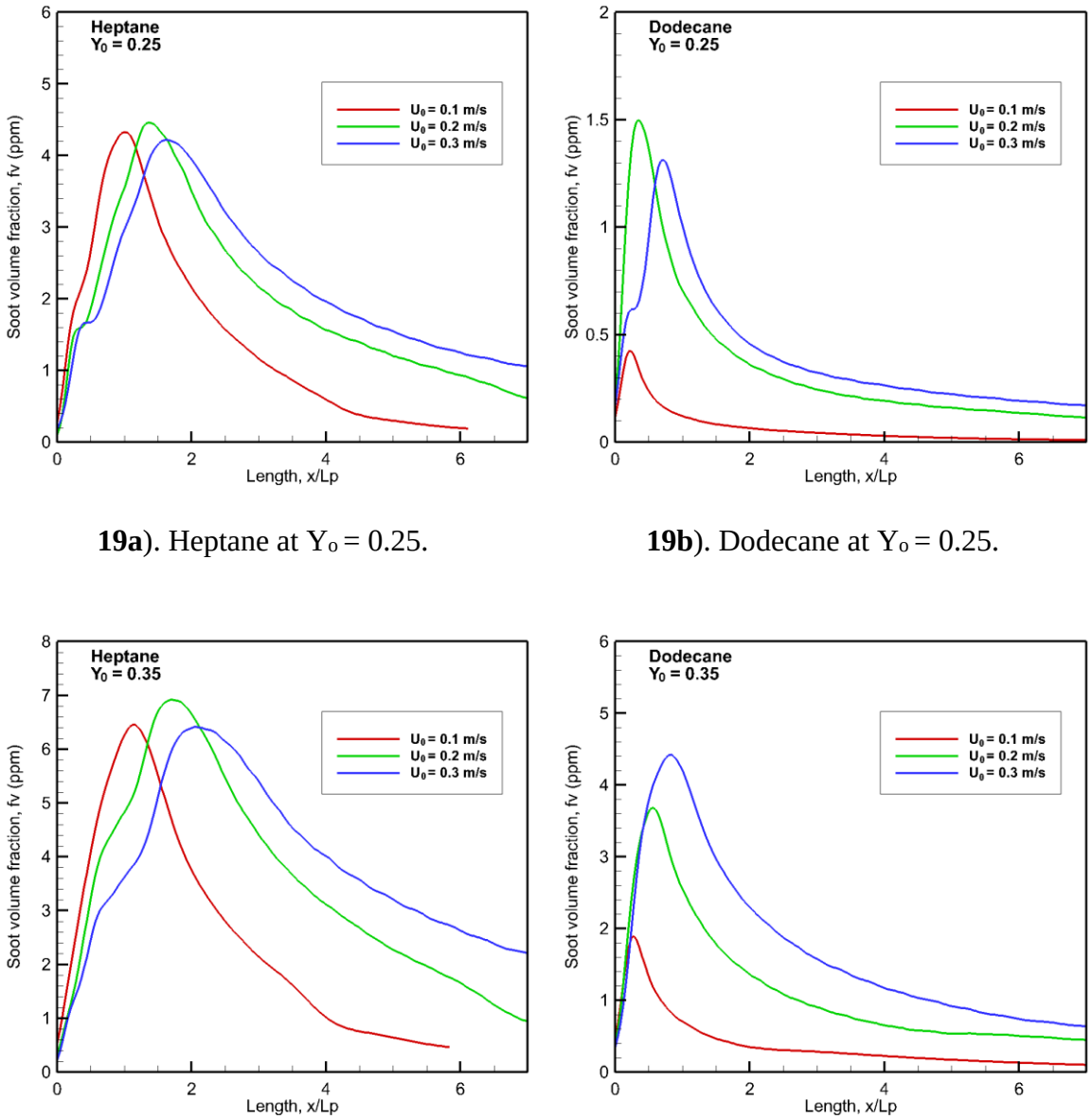

19a). Heptane at $Y_o = 0.25$.

19b). Dodecane at $Y_o = 0.25$.

19c). Heptane at $Y_o = 0.35$.

19d). Dodecane at $Y_o = 0.35$.

Figure 19. Evolution of the mean soot emission along the windward direction for different Y_o and U_0.

4. Conclusions

The overall research highlights the impact of the purely forced flow conditions, including oxygen concentration and flow speed, on a concurrent diffusion flame established over a liquid (heptane and dodecane) surface. Soot production within the viscous boundary layer at microgravity is reasonably well predicted with oxygen concentration below 0.35 by using the LSP model. Some major findings can be drawn from this numerical study as follows:

1) Near the leading edge of a low Reynolds number reacting flow, the greatest heat feedback results in a larger pyrolysis rate of liquid fuel. Both the visible flame length and soot emissions are rather sensitive to oxidizer velocities below those encountered in natural convection at Earth.
2) A decrease of both oxidizer flow velocity and oxygen concentration contributes to a reduction in soot formation as a consequence of a decrease of flame temperature.
3) Downstream of the leading edge, the concurrent diffusion flame gradually develops 3D features as a consequence of the oxygen side-transport induced by thermal expansion.
4) Fuel accumulation at the stoichiometric line results in a long visible flame length (T > 600 °C), particularly for heptane, with an increase in the visible flame length by a factor of 2.3 times in comparison with the dodecane flame.
5) The visible flame is thicker by a factor of about 9 times than that of the flame sheet at the stoichiometric line, independent on the flow conditions, including oxygen concentration and flow speed. As a result, the radiative loss fraction is above 0.5, which drives a decrease of flame temperature in comparison with an adiabatic one.
6) The pyrolysis rate is increasing with an augmentation of oxygen concentration and oxidizer flow velocity due to a rise of flame temperature. A peak of pyrolysis rate takes place near the leading edge with a drastically decreasing trend downstream, following the surface temperature trend. A strong pyrolysis rate of heptane results in an additional heat release by a factor of 2.5 times with an increase of oxidizer flow velocity from 0.1 to 0.3 m/s, and by a factor of only 25% with a rise of oxygen concentration from 0.25 to 0.35. The pyrolysis front of dodecane flame in low forced crossflow asymptotically reaches a limiting length.

Ongoing work aims to properly take into account a non-equilibrium model of liquid phase transition and the surface tension gradients induced by the temperature gradients. This allows us to predict flame spread at microgravity over thick heated liquid-phase flow.

Use of AI tools declaration

The authors declare they have not used Artificial Intelligence (AI) tools in the creation of this article.

Conflict of interest

The authors declare no conflict of interest.

References

1. Torero JL, Bonneau L, Most JM, et al. (1994) The effect of gravity on a laminar diffusion flame established over a horizontal plate, *25th Symposium (international) on Combustion (Pittsburgh: The Combustion Institute)*, 25: 1701–1709. https://doi.org/10.1016/S0082-0784(06)80818-0
2. Paul D Ronney (1998) Understanding combustion processes through microgravity research, *27th Symposium (international) on Combustion (Pittsburgh: The Combustion Institute)*, 27: 2485–2493. https://doi.org/10.1016/S0082-0784(98)80101-X

3. Olson SL, T'ien JS (2000) Buoyant low-stretch diffusion flames beneath cylindrical PMMA samples. *Combust Flame* 121: 439–452. https://doi.org/10.1016/S0010-2180(99)00161-3
4. Legros G, Joulain P, Vantelon JP, et al. (2006) Soot volume fraction measurements in a three dimensional laminar diffusion flame established in microgravity. *Combust Sci Technol* 178: 813–835. https://doi.org/10.1080/00102200500271344
5. Fuentes A, Legros G, Claverie A, et al. (2007) Influence of the oxidizer velocities on the sooting behaviour of non-buoyant laminar diffusion flame. *P Combust Inst* 31: 2685–2692.
6. Santa KJ, Chao BH, et al. (2007) Radiative extinction of gaseous spherical diffusion flames in microgravity. *Combust Flame* 151: 665–675. https://doi.org/10.1016/j.combustflame.2007.08.009
7. Konsur B, Megaridis CM, Griffin DW, et al. (1999) Soot aerosol properties in laminar soot-emitting microgravity nonpremixed flames. *Combust Flame* 118: 509–520. https://doi.org/10.1016/S0010-2180(99)00021-8
8. Tyurenkova VV, Smirnova MN (2023) Analytical approach to flame propagation over thermally destructing structured material problem. // Acta Astronautica, Pergamon Press Ltd. (United Kingdom), 213: 438–445. https://doi.org/10.1016/j.actaastro.2023.09.020
9. Tyurenkova VV, Stamov LI (2019) Flame propagation in weightlessness above the burning surface of material. *Acta Astronaut* 159: 342–348. https://doi.org/10.1016/j.actaastro.2019.03.053
10. Rouvreau S, Torero JL, Joulain P (2005) Numerical evaluation of boundary layer assumptions for laminar diffusion flames in micro gravity. *Combust Theor Model* 9: 137–158. https://doi.org/10.1080/13647830500098381
11. Fernandez-Pello AC (1979) Flame spread in a forward forced flow. *Combust Flame* 36: 63–78. https://doi.org/10.1016/0010-2180(79)90046-4
12. Fernandez-Pello AC, Mao CP (1981) A unified analysis of concurrent modes of flame spread. *Combust Sci Technol* 26: 147–155. https://doi.org/10.1080/00102208108946954
13. Ferkul PV, Y'ien JS (1994) A model of low-speed concurrent flow spread over a thin fuel. *Combust Sci Technol* 99: 345–370. https://doi.org/10.1080/00102209408935440
14. Li C, Liao YTT, James S, et al. (2019) Transient flame growth and spread processes over a large solid fabric in concurrent low-speed flows in microgravity – Model versus experiment. *Proc Combust Inst* 37: 4163–4171. https://doi.org/10.1016/j.proci.2018.05.168
15. Urban DL, Ferkul P, Olson S, et al. (2019) Flame spread: Effects of microgravity and scale. *Combust Flame* 199: 168–182. https://doi.org/10.1016/j.combustflame.2018.10.012
16. Tseng YT, T'ien JS (2010) Limiting length steady spread and nongrowing flames in concurrent flow over solids. *J Heat Transfer* 132: 091201. https://doi.org/10.1115/1.4001645
17. Zhao X, Liao YTT, Johnston MC, et al. (2017) Concurrent flame growth, spread, and quenching over composite fabric samples in low speed purely forced flow in microgravity. *Proc Combust Inst* 36: 2971–2978. https://doi.org/10.1016/j.proci.2016.06.028
18. Mell WE, Kashiwagi T (2000) Effects of finite sample width on transition and flame spread in microgravity. *Proc Combust Inst* 28: 2785–2792. https://doi.org/10.1016/S0082-0784(00)80700-6

19. Guibaud A, Consalvi JL, Orlac'h JM, et al. (2020) Soot production and radiative heat transfer in opposed flame spread over a polyethylene insulated wire in microgravity. *Fire Technol* 56: 287–314. https://doi.org/10.1007/s10694-019-00850-8
20. Wen Z, Yun S, Thomson MJ, et al. (2003) Modeling soot formation in turbulent kerosene/air jet diffusion flames. *Combust Flame* 135: 323–340. https://doi.org/10.1016/S0010-2180(03)00179-2
21. Lui F, Guo HS, Gregory J, et al. (2002) Effects of gas and soot radiation on soot formation in a coflow laminar ethylene diffusion flame. *J Quant Spectrosc Radiat Transf* 73: 409–421. https://doi.org/10.1016/S0022-4073(01)00205-9
22. Leung KM, Lindstedt RP, Jones WP (1991) A simplified reaction mechanism for soot formation in nonpremixed flames. *Combust Flame* 87: 289–305. https://doi.org/10.1016/S0022-4073(01)00205-9
23. Vovelle C, Delfan JL, Reuillon M (1994) Formation of Aromatic Hydrocarbons in Decane and Kerosene Flames at Reduced Pressure. In: *Bockhorn, H. (eds) Soot Formation in Combustion. Springer Series in Chemical Physics*, 59. Springer, Berlin, Heidelberg. https://doi.org/10.1007/978-3-642-85167-4_4
24. Anderson H, McEnally CS, Pfefferle LD (2000) Experimental study of naphthalene formation pathways in non-premixed methane flames poped with alkylbenzenes, *28th Symposium (international) on Combustion (Pittsburgh: The Combustion Institute)*, 2577–2585. https://doi.org/10.1016/S0082-0784(00)80675-X
25. Hall RJ, Smooke MD, Colket MD (1997) *Physical and Chemical Aspects of Combustion, A Tribute to Irvine Glassman*, F.L Dryer and R.F Sawyer (Ed.) Gordon & Breach, 189.
26. Beji T, Zhang JP, Delichatsios M (2008) Delichatsios, Determination of soot formation rate from laminar smoke point measurements. *Combust Sci Technol* 180: 927940. https://doi.org/10.1080/00102200801894398
27. Mcgrattan K, Mcdermott R, Hostikka S, et al. (2018) Fire Dynamics Simulator (Version 6), User's guide, NIST Special Publication.
28. Andersen J, Rasmussen CL, Giselsson T, et al. (2009) Global combustion mechanisms for use in CFD modeling under oxy-fuel conditions. *Energ Fuel* 23: 1379–1389. https://doi.org/10.1021/ef8003619
29. Murty KA (1975) Introduction to Combustion Phenomena, New York: Gordon, ISBN 0–6.
30. Wang HY, Merino JLF, Dagaut P (2011) Effects of soot formation on shape of a nonpremixed laminar flame established in a shear boundary layer in microgravity. *J Phys* 327: 012038. https://doi.org/10.1088/1742-6596/327/1/012038
31. Emmons HW (1956) The film combustion of liquid fuel. *Z Angew Math Mech* 36: 60–71. https://doi.org/10.1002/zamm.19560360105
32. Schlichting H (1979) *Boundary layer theory*, Seventh Edition, McGraw-Hill.
33. Fujita O, Ito K, Ito H, et al. (1997) Effect of thermophoretic force on soot agglomeration process in diffusion flame under microgravity, *4th NASA International Microgravity Combustion Workshop*, 217–222.